Ukoba, Kingsley; Akinribide, Ojo J.; Adeleke, Oluwatobi; Akinwamide, Samuel O.; Jen, Tien Chien; Olubambi, Peter A.

Structural integrity and hybrid ANFIS-PSO modeling of the corrosion rate of ductile irons in different environments

Published in:
Kuwait Journal of Science

DOI:
10.1016/j.kjs.2024.100234

Published: 01/07/2024

Document Version
Publisher's PDF, also known as Version of record

Kuwait Journal of Science 51 (2024) 100234

Contents lists available at ScienceDirect

Kuwait Journal of Science

journal homepage: www.sciencedirect.com/journal/kuwait-journal-of-science

Full Length Article

Structural integrity and hybrid ANFIS-PSO modeling of the corrosion rate of ductile irons in different environments

Kingsley Ukoba [a,*], Ojo J. Akinribide [b], Oluwatobi Adeleke [a], Samuel O. Akinwamide [c], Tien-Chien Jen [a], Peter A. Olubambi [b]

[a] Department of Mechanical Engineering Science, University of Johannesburg, Cnr Kingsway and University Roads, Auckland Park, 2092, Johannesburg, South Africa
[b] Centre for Nanoengineering and Advanced Materials, University of Johannesburg, Doornfontein, Johannesburg, South Africa
[c] Department of Mechanical Engineering, Aalto University, Espoo, Finland

ARTICLE INFO

Keywords:
Corrosion
Inhibitor
Machine learning
ductile iron
ANFIS-PSO
Weight loss

ABSTRACT

Ductile iron (DI) samples were immersed in near-neutral, alkaline sodium hydroxide (NaOH), and sodium chloride (NaCl) environments for 180 days. The influence of microstructure on the corrosion resistance of three DI specimens was investigated. Microstructures, electrochemical measurements, and the characterization of the corroded surfaces were analyzed. The experimental results from this study were used to validate a model generated from hybrid adaptive neuro-fuzzy inferences system-particle swarm optimization (ANFIS-PSO) algorithms. The hybrid ANFIS-PSO modelling technique was improvised for a detailed evaluation of corrosion rate of ductile cast iron materials in different environments. The integrated hybrid ANFIS-PSO model revealed a sharp rise in localized corrosion caused by chloride-induced structural deterioration at the nanoscale for some of the grains. The performance results revealed that the fuzzy c-mean (FCM) clustering outperformed other clustering approach in the neuro-fuzzy model. Accuracy values of 92.9% and 93.7% were recorded for the training phase of ANFIS-FCM and ANFIS-PSO-FCM respectively for corrosion rates. The percentage error of the ANFIS-PSO predictions is significantly lower than the ANFIS-standalone prediction. This shows that the ANFIS-PSO with FCM approach is a better model for predicting corrosion rates. This will contribute to the body of knowledge for ductile iron, corrosion, and corrosion modelling using machine learning.

1. Introduction

Social economic losses could be held responsible for the majority of government losses in well-known global industries. According to Wasim et al. (2020a) and Zheng et al. (2020) materials made with ductile iron components are at the forefront of these failures. An in-depth analysis by the United States on the economic impact of corrosion reveals that materials made of ductile iron constituents incur the highest cost in terms of percentage losses in repair and maintenance services (Koch et al., 2005). According to the literature, the United States has been employing ductile cast iron for water pipelines since the 1960s. However, due to the prolonged period of use as a method of transporting water across states, these pipelines now require frequent maintenance and repair (Koch et al., 2005; Szeliga et al., 2003). The failure of these materials in service conditions has been attributed to the harsh environment in which they find their application (Wasim et al., 2018).

One of the innovators who initiated a thorough corrosion assessment of materials made from DI constituents such as wheels, gearboxes, buried water pipelines, and engine seats in the US was Romanoff (1957). To test how different environments and environmental factors would affect these materials, he submerged numerous sections of DI pipe in various environments. However, the model created by Romanoff's research lacked validation due to the variances and uncertainties in field conditions. The analysis of DI pipes by Kleiner et al. (2012) stands out among the many field studies on the corrosion of DI materials conducted after Romanoff's works. In North America, Kleiner et al. (2012) studied several excavated DI materials and the influence of the environment on their properties. The information gathered from the 3D scan test conducted for the detection of corrosion pits was used to perform a statistical analysis of geometry and pit scattering. The study also provided a method based on corrosion pit geometry for assessing the susceptibility of DI materials to environmental degradation. According to the literature, limited research exists on the corrosion properties of DI materials exposed to environments capable of causing accelerated deterioration.

* Corresponding author.
E-mail address: akinribideojo@yahoo.com (K. Ukoba).

https://doi.org/10.1016/j.kjs.2024.100234
Received 11 September 2023; Received in revised form 8 April 2024; Accepted 21 April 2024
Available online 23 April 2024

Recent research has compared the effects of chloride environment on DI and carbon steels (Song et al., 2017). Specimens from this study were subjected to electrochemical corrosion tests, physical mass loss, pit depth, surface morphology, and examination of the corrosion products. The findings from the three-month corrosion test showed that DI is more resistant to corrosion than mild steel in different environment such as near neutral, NaCl, NaOH and soils activated with different chloride proportions.

Moreover, corrosion studies on DI in near-neutral environments has been investigated using techniques such as cathodic protection, surface analysis, and corrosion product characterization (You et al., 2020). The rapid corrosion of DI was reportedly resulted from the high salt concentration in the chloride environment compared to other environments. However, this study was performed within a short period; hence, mass loss measurement was not reported. However, this study did not examine how the mechanical properties of the DI would be influenced by corrosion. Similar experiments by Wang et al. (2019) and Ochoa et al. (2022) were conducted to assess the effect of corrosive environments on the mechanical and microstructural properties of grey cast iron. Their findings show that an acidic environment caused a decline in the tensile and fracture toughness of the specimens, while a chlorinated alkaline environment resulted in galvanic coupling between electrochemically nobler graphite particles and the matrix.

The current research reports the corrosion findings on DI after 180 days of exposure. Weight loss and corrosion rate analyses were performed experimentally to understand how the mechanical properties of the DI specimens were affected by different corrosive environments. ANFIS-PSO modelling technique was adopted to compare the experimental values and the modelled results. In addition to these measurements, optimal hybrid ANFIS-PSO model building and parameter optimization analysis was employed to validate results obtained after 180 days to see the effect of corrosion on the predominant ferrite phase. A flowchart describing the experimental and modeling process in this research is presented in Fig. 1.

2. Materials and methods

2.1. Specimen design

The ductile iron (DI) samples used in this study were acquired from the Engineering Materials Development Institute (EMDI) in Nigeria, and their elemental composition is presented in Table 1. Equipment such as cutting machine, computer numerical control (CNC) machine were used to mechanically shape the specimens to precise dimensions of 20 mm (length), 10 mm (width), and 6 mm (thickness). Samples for analysis were vertically projected and completely immersed in a near-neutral alkaline sodium hydroxide (NaOH) and sodium chloride (NaCl) environments to determine their corrosion susceptibility in these environments. To simulate actual service conditions, contact between the specimen and the wall of the container was prevented. The initial weights of the polished specimens were recorded before undergoing laser cleaning to remove the corroded surface.

2.2. Morphological examination and mechanical testing

Detailed morphological characterization was performed on the ductile iron (DI) samples to examine their internal structures using a JSM-6700F scanning electron microscope (SEM), and phase identification was carried out using a Rigaku X-ray diffraction machine operating at a diffraction angle range between 30^0 and 80^0. A universal mechanical testing machine with model number 3309 was used to conduct the tensile test on the three samples immersed in the test environment. Three samples were selected and immersed in each environment to ensure repeatability and reproducibility of values. Fractographic evaluation of the samples was performed using SEM to examine the mode of fracture of samples immersed in different environments. Micro hardness test was conducted on each sample and repeated thrice to ensure the reliability of the hardness values before applying the ANFIS and ANFIS-PSO to predict the outcome of both tensile and the hardness results.

2.3. Environments

To estimate the variations in results arising from the heterogeneity of the environment provided, 5 mol of aqueous sodium chloride (NaCl), Sodium hydroxide (NaOH), and a near-neutral environment with respective pHs of 6.8, 7 and 7.4 were employed in the testing rather than the real environments. The chemical composition of the chloride environment is presented in Table 2. These environments were chosen in this study because previous research had shown their ability to rapidly deteriorate metallic components (Wasim et al., 2017, 2020b).

2.4. Rates of corrosion

Three identical samples with the same geometry were used in each test environment, and the weight of the specimens before and after corrosion was measured to evaluate the corrosion rates. After 180 days of immersion in the test environments, the samples were removed for weight loss assessments. According to the approved ASTM G1-03 standard (2017) (Astm and Practice for Preparing; Joseph et al., 2021), the deteriorated samples were chemically rinsed in Clark's solution for a minute to remove the corrosion products without modifying the surface of the specimens. The specimens were cleaned, dried and weighed to determine the weight loss according to Equation (1).

$$W_T = W_i - W \tag{1}$$

Where W_T = resultant weight loss of the sample, W_i = initial weight of the sample, and W_f = weight after removal of corrosion products. The corrosion rate is evaluated from the resultant weight loss values according to Equation (2).

$$C.R = (\gamma) * W_T / (A * (T) * \delta) \tag{2}$$

Where C.R = corrosion rate, γ = constant (87600), WT = resultant weight, A = covered area, T = time of exposure, and δ = theoretical density.

It should be noted that mass loss measurement used to assess corrosion degradation in the ductile iron specimens was employed in a previous study to evaluate the corrosion rate in aggressive environments (Davis, 2000). Fig. 2 illustrates the corrosion setup used in this study.

2.5. Adaptive neuro-fuzzy inference system

The adaptive neuro-fuzzy inference system (ANFIS) is a framework which was first developed by Jang, 1993a, 1993b and integrated the fuzzy if-then rule system and numerical methods of artificial neural network forming a robust neuro-fuzzy system (Lazreg et al., 2022). The fuzzy if-then rule system is characterized by membership functions (MF) that optimize the linear consequent and non-linear premise parameters (Rajaobelina et al., 2022). The choice of functions such as Gaussian, triangular, trapezoidal, and sigmoidal, amongst others, are dependent on the nature of the problem to be solved. The fuzzy module in the fuzzy system mathematically maps the crips input to the fuzzy sets designated by the membership function, $\mu \in [0,1]$ (Seifi et al., 2022). ANFIS consists of a fuzzy layer (input layer), product layer, normalization layer, defuzzification and summation layer, as represented in Fig. 3. At the first layer, called the fuzzy layer, the membership grade containing the input and output functions at each node is computed, while the multiplication of the signal for the input in each layer is computed in the second layer (product layer). At the normalization layer, the output is a fraction of the firing strength of the node to the sum of all firing strength of the other nodes, while the signal from the normalization layer is multiplied by the fuzzy rule's function at the defuzzification layer. The total output is

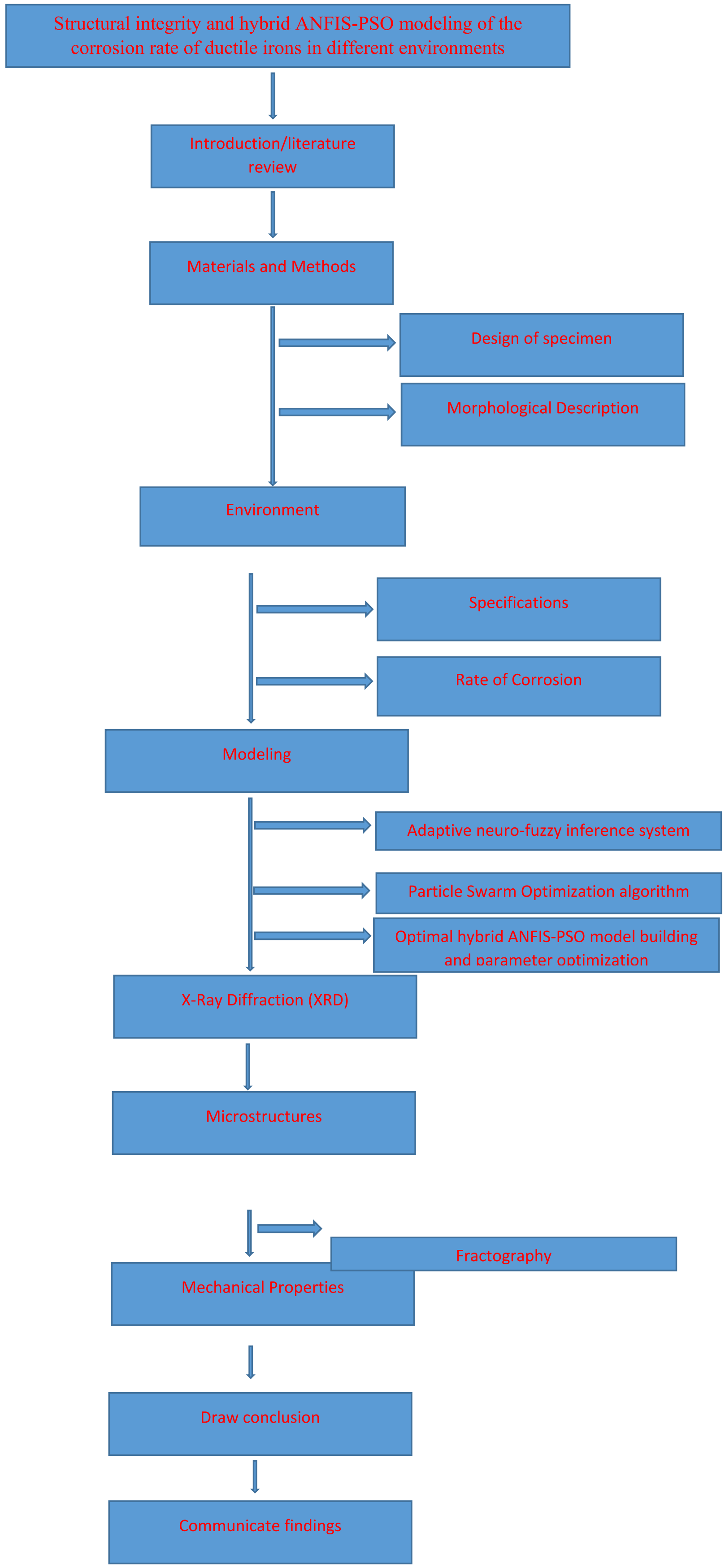

Fig. 1. Design of study flow chart.

Table 1
The compositions (weight percentage) of indigenously produced ductile iron.

Si	P	Cr	C	Mn	S	Mg	Sn	Pb	Cu	Fe
2.7	0.04	0.12	3.7	0.4	0.03	0.055	0.02	0.0015	0.1	92.8

Table 2
Composition of the chloride environment used (Wasim et al., 2020b; Koneshan et al., 2000) Na^+–water, Cl^-–water, ion–ion, and water–water potential parameters.

Ion δ_{i0}(Å) ε_{i0} (kJ/mol) δ_{ih}(Å) ε_{ih} (kJ/mol)				
Na^+	2.72	0.560 14	1.310	0.560 14
Cl^-	3.55	1.505 75	2.140	1.505 75
Ion pair δ(Å) ε (kJ/mol)				
Na^+ Na^+	2.443	0.119 13		
Na^+ Cl^-	2.796	0.352 6		
Cl– Cl^-	3.487	0.979 06		
Water δ_{00}(Å) ε_{00} (kJ/mol) Charge (q)				
O(H_2O)	3.156	0.650 20	−0.82	
H(H_2O)			+0.41	

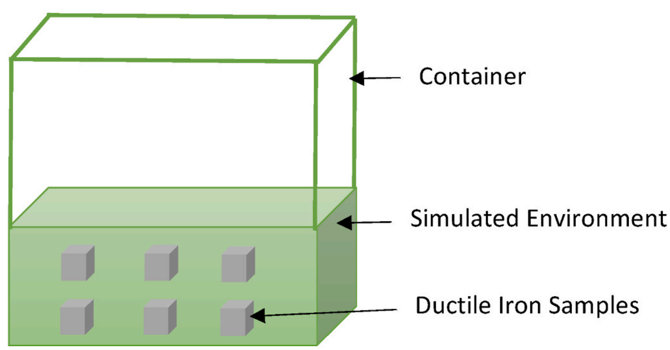

Fig. 2. Schematic diagram of the corrosion setup in different environments.

estimated at the summation (output layer) by adding all signals from all layers using a summation function. The Takagi–Sugeno fuzzy technique in the ANFIS controller is depicted by a rule-based system with two inputs, a and b, and one output in a fuzzy inference system.

$$\text{Rule 1 : If } a \text{ is } A_1 \text{ and } b \text{ is } B_1, F_1 = S_1 a + r_1 b + t_1 \tag{3}$$

$$\text{Rule 2 : If } a \text{ is } A_2 \text{ and } b \text{ is } B_2, F_2 = S_2 a + r_2 b + t_2 \tag{4}$$

Where A_1, A_2, B_1, B_2 represent the membership functions while a and b are input parameters. F_1 *and* F_2 are acquired outputs from the system, whereas $s, r,$ and t are nodal consequent parameters.

2.6. Particle swarm optimization algorithm

Particle swarm optimization (PSO) was initially developed by Eberhart and Kennedy (Eberhart et al., 1995) as well as Seifi et al. (2022) to stimulate the social behavior of animals like bird populations and fishes. The PSO is a computational approach which is used for the optimization of problems iteratively such that a population of candidate solutions is improved based on identified quality measures, moved in a space over its position and velocity (Adeleke et al., 2022a). The working principle of PSO is simplified in three basic steps, generating the positions and velocities, updating the position and updating the velocities. The position of the particles is updated using the velocities of the particles, while the position denotes the prospective solutions in the search space (Li et al., 2022). The position (x_i) and velocity (v_i) of the *ith* particle are arranged based on their best local positions and the global positions in the search ranges and updated iteratively using the following equations:

$$v_i(k) = \omega v_i(k-1) + r_1 c_1 (x_{Pbest} - x_i(k)) + r_2 c_2 (x_{Gbest} - x_i(k)) \tag{5}$$

$$x_i(k) = x_i(k-1) + v_i(k) \tag{6}$$

$$\omega = \omega_{damp} \times \omega \tag{7}$$

Above, c_1 *is* positive cognitive acceleration coefficient, c_2 *is* social acceleration coefficient, r_1 and r_2 are uniformly distributed random variables between 0 and 1, ω is inertia weight, and ω_{damp} is the weight-damping ratio. In this study, the PSO optimization algorithm is explored to tune the parameters of the 1st and 4th adaptive layers of the standalone ANFIS such that local minima are avoided.

2.7. Optimal hybrid ANFIS-PSO model building and parameter optimization

The hybrid neuro-fuzzy model was developed in this study based on data samples extracted from the experimental procedures and set as the input and output variables for the model. Input variables comprise exposure time, environment and weight loss, while the output variables are corrosion rate, hardness and tensile strength. The entire data set was divided in two: 70% was selected for training, while the remaining 30% was used to establish the accuracy and reliability of the developed model. Due to the significance of data preprocessing in the improvement and performance of the neuro-fuzzy model, it is essential to ensure that the training data falls within the range of 0 and 1. The normalization of the training data was performed using Equation (8).

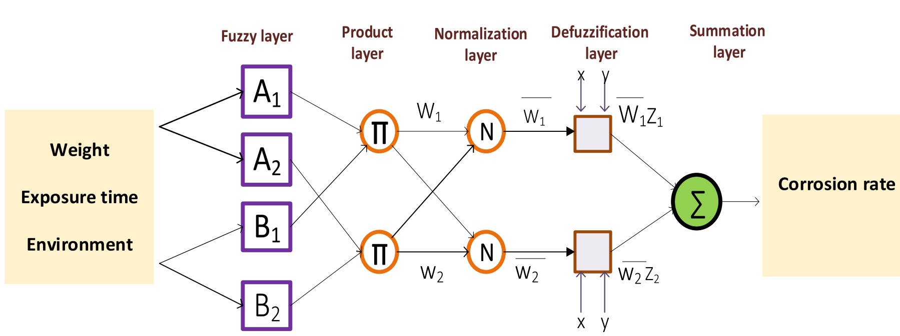

Fig. 3. Adaptive neuro-fuzzy inferences system (ANFIS) model architecture.

$$y_{norm} = \frac{x - x_{min}}{x_{max} - x_{min}} \tag{8}$$

where y_{norm} = the normalized data, x = the mean of the variable, x_{min} = minimum variable, xmax = maximum variable.

The significance of hybridization in tuning the parameters of the ANFIS model using evolutionary algorithm PSO for improved performance of the ANFIS model was established in this study. The choice of hyper-parameters of the ANFIS models and PSO algorithms is critical to the accuracy of the model, thus, careful selection of the control parameters of ANFIS and PSO was considered in this study. Clustering is a crucial requirement in neuro-fuzzy modelling for grouping data points into a similar fuzzy cluster, assigning membership functions and generating a fuzzy inference system structure for the data. In this study, fuzzy c-means (FCM) clustering is preferred over other techniques due to its speed boost capacity (Bamgbade et al., 2022). The parameters set for the ANFIS and PSO algorithm is presented in Table 3.

The competence, reliability and eligibility of the developed ANFIS and ANFIS-PSO models for the prediction of the corrosion rates, hardness and tensile strength based on weight loss approach were established by comparing the experimental and predicted values using relevant statistical metrics. The best models were selected after testing their performance using mean absolute percentage error (MAPE), mean absolute deviation (MAD), root mean square error (RMSE), and correlation coefficient (R^2) were computed using equations (9)–(12) respectively.

$$MAPE = \frac{1}{N}\sum_{i=1}^{N}\left|\frac{O_i - P_i}{O_i}\right| x\ 100\% \tag{9}$$

$$MAD = \sum_{i=1}^{N}\frac{(O_i - P_i)}{N} \tag{10}$$

$$RMSE = \left(\sum_{i=1}^{N}\frac{(P_i - O_i)^2}{N}\right)^{1/2} \tag{11}$$

$$R^2 = 1 - \left[\frac{\sum_{i=1}^{n}(O_i - O)(P_i - P)}{\sqrt{\sum_{i=1}^{n}(O_i - O)^2\ x \sum_{i=1}^{n}(P_I - P)^2}}\right]^2 \tag{12}$$

Where n represents the number of samples, i = the sample index, P_i the value of the predicted outcome for ith sample, O_i the experimental outcome for the ith sample, O the average experimental outcome, and P the average predicted outcome.

3. Results and discussion

3.1. X-ray diffraction

To analyze the corrosion morphology on the surface of ductile iron samples immersed in the three different environments, the X-ray diffractometer (XRD) analysis was used to ascertain the corrosion products of the samples removed from the three test environments. Fig. 4 below displays the XRD analysis of the specimens after 180 days of immersion. The $C_{0.07}Fe_{1.93}$ phase with plane orientation γ[200] belongs to the martensite phase with traces of magnetite (Fe_2O_3). Moreover, the segregated chromium nickel iron phase (Cr–Ni–Fe–C) with plane orientation α [211] comprised the bulk of the corrosion product observed in the specimens, as presented in Fig. 4.

Additionally, a quantitative approach to the corrosion products was carried out, which showed that 90 % of them were martensite that was porous, and the remaining 10% were magnetite consisting of a ferritic phase. For the ductile irons, martensite predominance has been discovered in comparison to the selected environments (Wasim et al., 2019a). The production of a significant amount of $C_{0.07}Fe_{1.93}$ on the samples shows that in all environments, the pH solution contains a significant amount of ions (Song et al., 2017). $C_{0.07}Fe_{1.93}$ martensite and Cr–Ni–Fe–C ferrite with γ[200] and α[211] were shown to be the primary corrosion products on all the ductile iron subjected to different solutions in a recent corrosion research (Qin et al., 2018; Krawiec et al., 2021). Stages found in the rust layers caused by corrosion. After exposing the selected ductile irons to the different solutions including Cl and OH^-, Na^+, corrosion products, in a two-layer structure consisting of martensite and magnetite were also noted. High Cl concentration favors the development of martensite phase (Zhang et al., 2011).

3.2. Microstructural description of ductile iron

The images displayed in Fig. 5 shows the optical micrographs of the sample used for the corrosion analysis before immersed in three different corrosion media. From the results of the optical images, spheroidal graphite is seen to be relatively distributed throughout the entire micrographs. The grain boundaries are connected in a network form surrounding the spheroidal graphite nodules. The sizes of graphite nodules observed in sample prepared for immersion in sodium hydroxide environment has some relatively low amount of martensite present in the entire micrograph.

3.2.1. Scanning electron microscopy

The micrographs presented in Figs. 6–8 represents the morphology of the DI specimens before corrosion. From Fig. 4, it is observed that the microstructures contain some pearlite, ferrite and uniformly distributed spheroidal graphite in the entire matrix of ductile iron. The ferritic phase was found enveloping the spheroidal graphite nodules. The homogeneously distributed graphite nodules covered the whole ductile iron. There is a clear separation observed in the ferrite phase which forms the entire block of martensite within the ductile iron matrix of each sample. The morphological characteristic of the ductile iron immersed in sodium hydroxide environment form some acicular martensite which are very large in sides and in distinct form as displayed in Fig. 6. The mechanisms of corrosion observed in all the microstructures shows that the structural morphology of the samples after the weight loss test indicates some pitting and evidence of large corrosion holes was observed in all the sample after corrosion.

The corroded samples show some corrosion attack which is due to enlargement of corrosion pits appearing in some segregated sections of the samples. This is clearly attributed to pitting form of corrosion. Due to some atom-rich and atom-poor-regions on the corroded samples, there was a strong segregation of the microstructural surface forming cladding layers. Inconsistency was observed on the microstructure of each sample after immersed in NaOH, NaCl, and the near-neutral media due to inhomogeneous experienced during the corrosion process. Comparing the corrosion products observed on each sample in Figs. 6 and 7, we observed the absence of pits on the surface of the sample immersed in near-neutral environment. which depicts less corrosion in comparison with samples immersed in other environments. The presence of boride and carbide in the corrosion products could be responsible for

Table 3
Specified parameters for ANFIS and PSO algorithms.

Parameter		Value
ANFIS	FIS structure	Takagi-Sugeno-type
	FIS function	genfis3
	Number of clusters	5
	Maximum iteration	100
	Minimum improvement	1e-5
	Number of exponents for matrix portioning	2
	Stopping criteria	Max no of iterations
PSO algorithm	Initial swarm size	20
	Initial weight, ω	0.5
	Initial weight damping ratio, ω_{damp}	0.8
	Social acceleration co-efficient, c_1	2
	Cognitive acceleration co-efficient, c_2	2

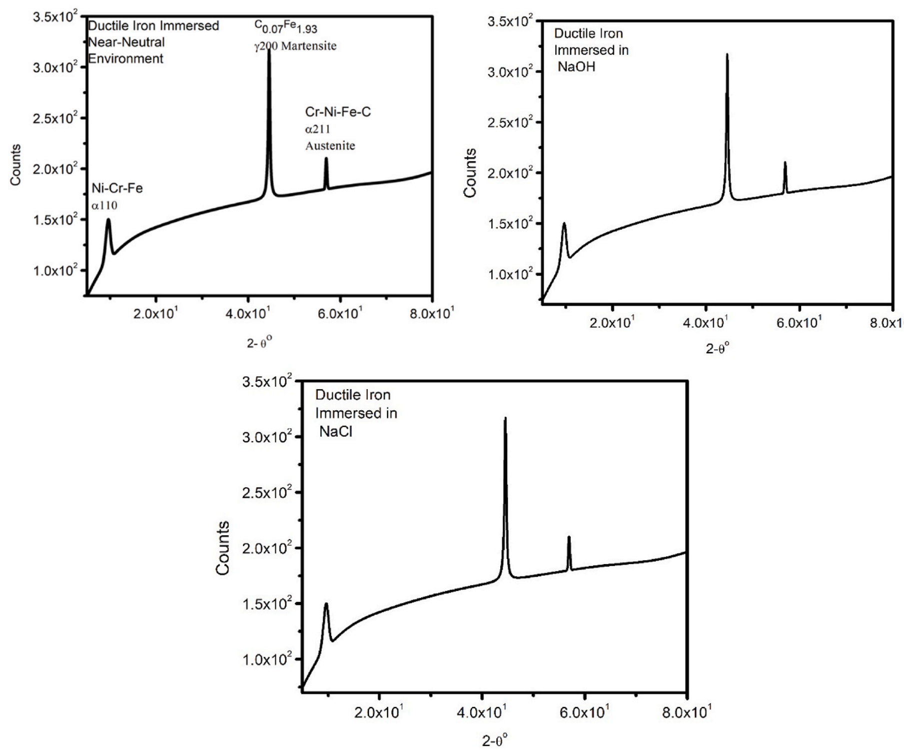

Fig. 4. The crystallographic analysis of ductile iron immersed in near neutral, sodium hydroxide, and sodium chloride environments.

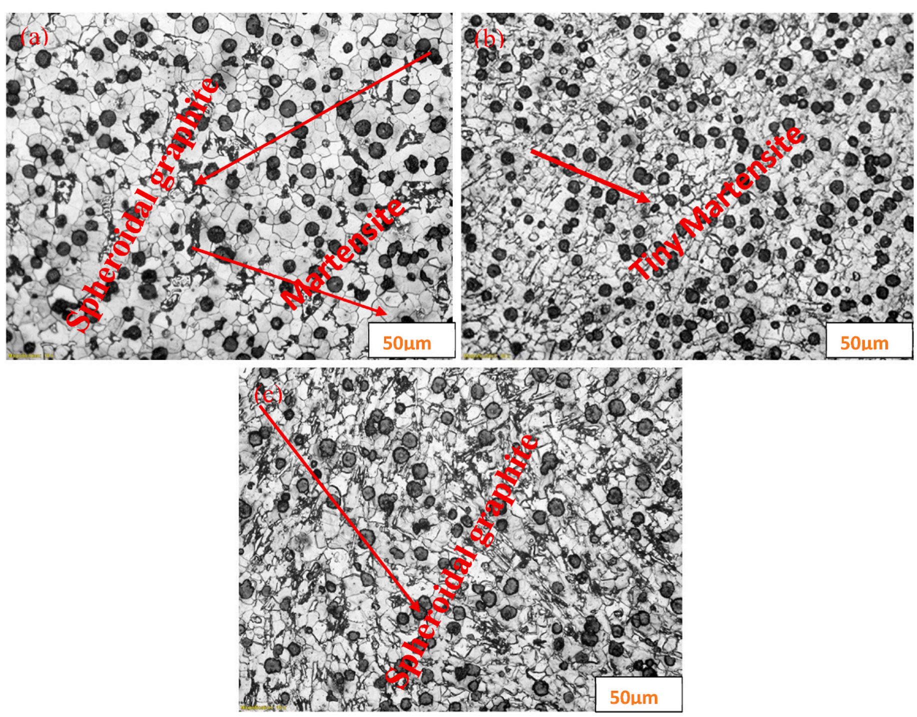

Fig. 5. Optical images of ductile iron immersed in (a) near – neutral environment, (b) sodium hydroxide NaOH environment, and (c) sodium chloride NaCl environment.

prevention of aggravated corrosion products on the samples. A clear network of block like continuous structure was noticed in samples displayed in Figs. 6b, 7b and 8b.

3.3. Fractographic analysis of ductile irons

The fracture morphology analysis of ductile iron immersed in NaCl, NaOH, and near-neutral environments in Fig. 9 offers critical insights into the material's behavior under different chemical conditions. Ductile iron, known for its strength and ductility, can exhibit distinct fracture

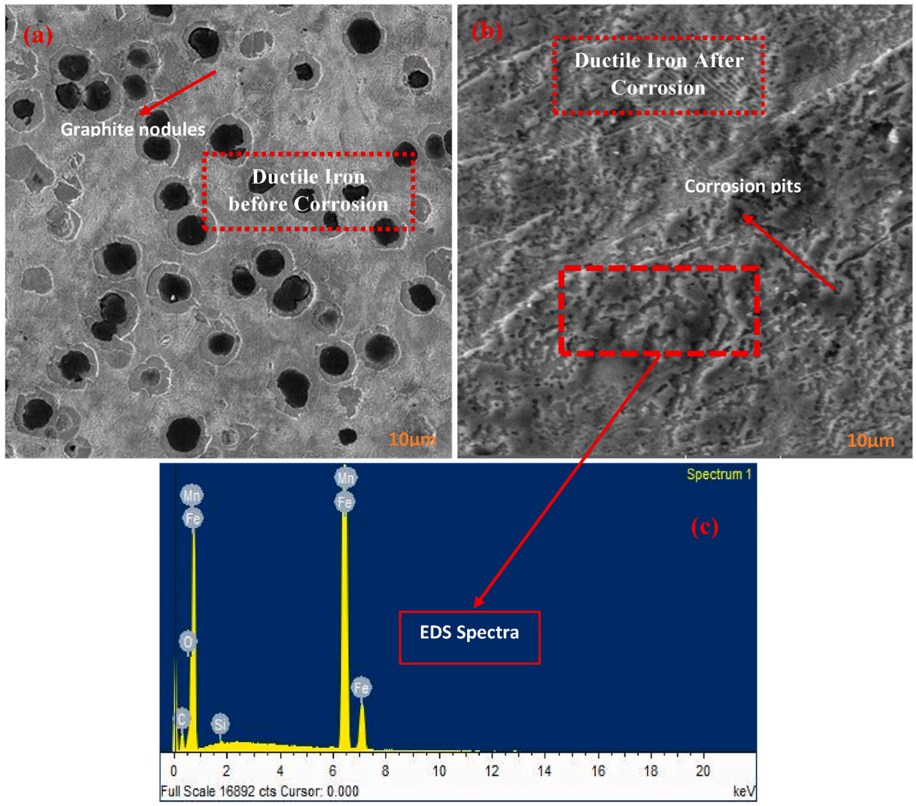

Fig. 6. Microstructural analysis of ductile iron prepared for near-neutral environment (a) before corrosion, (b) after corrosion and (c) energy dispersion spectroscopy analysis EDS-Spectra.

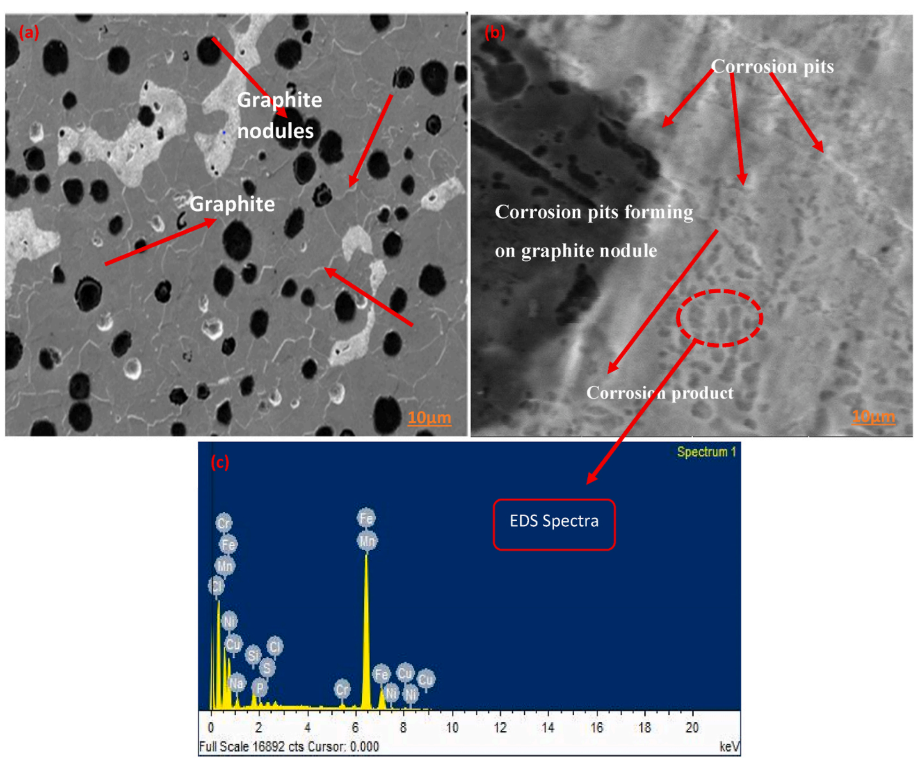

Fig. 7. Microstructural analysis of ductile iron preparation for NaOH environment (a) before corrosion, (b) after corrosion and (c) energy dispersion spectroscopy analysis EDS-Spectra.

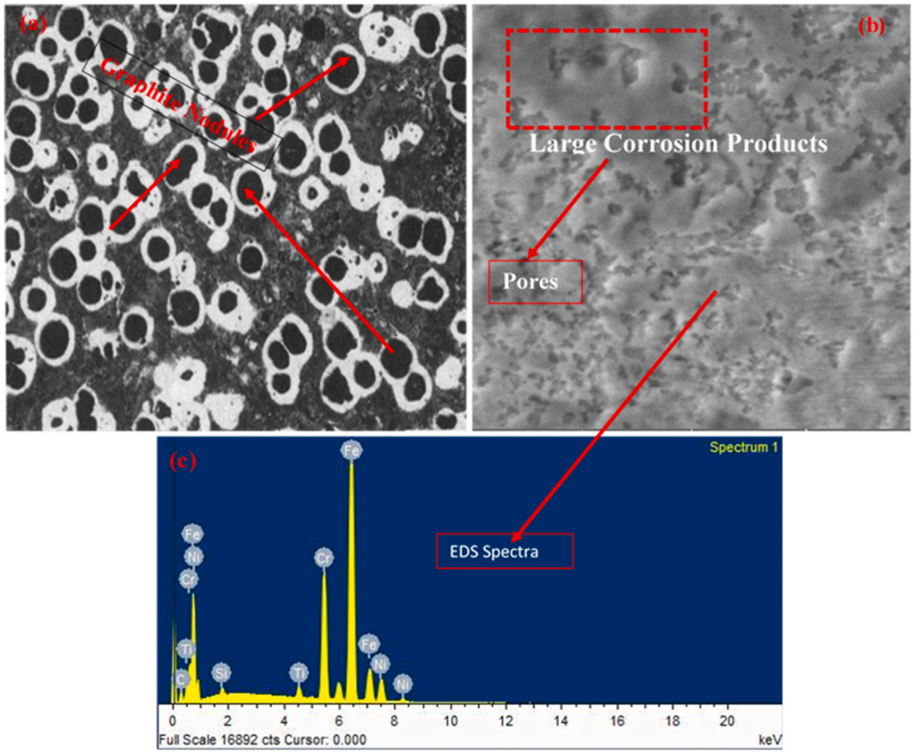

Fig. 8. Microstructural analysis of ductile iron preparation for NaCl environment (a) before corrosion, (b) after corrosion, and (c) energy dispersion spectroscopy analysis EDS-Spectra.

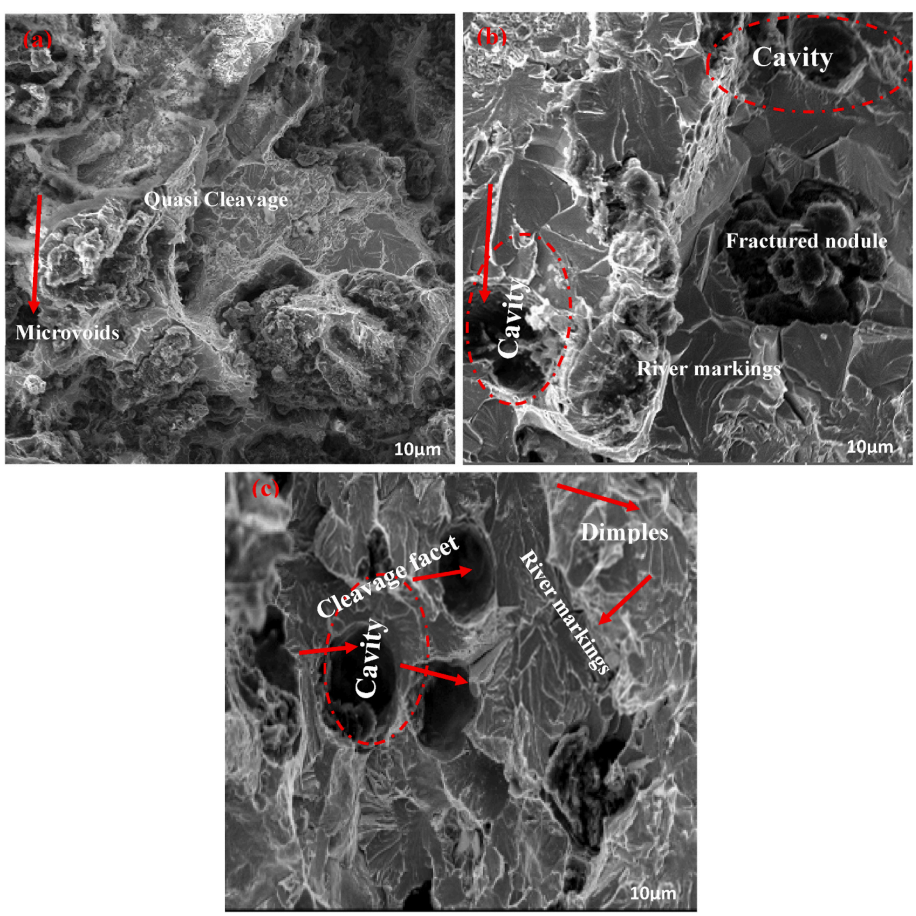

Fig. 9. Fractography images of ductile iron specimens immersed in (a) NaCl (b) NaOH, and (c) near neutral environment.

features depending on the type and severity of the environment it encounters according to Labrecque and Gagne (Labrecque et al., 1998). The results of fracture morphology presented in Fig. 9 shows some mode of fracture observed in the three samples, and they are thoroughly analyzed via SEM.

The DI immersed in a sodium chloride solution, faces the corrosive challenge posed by chloride ions, making it susceptible to chloride-induced defects such as pitting corrosion. The chloride ions penetrate the protective oxide layer on the specimen surface, leading to the formation of ferrous chloride complexes, quasi cleavage fracture and accelerating the corrosion process as seen in Fig. 9a. Fractured surfaces of DI subjected to corrosion in NaCl solutions often exhibit characteristic features such as transgranular cracking, crack propagation along grain boundaries, and intergranular attack due to prolonged exposure in the corrosive NaCl environment. The presence of secondary cracks and microvoids within the fracture surface suggests the synergistic effects of chloride-induced corrosion.

The fracture micrograph of specimen immersed in NaOH solution shown in Fig. 9b reveals that the specimen undergoes different corrosion mechanisms, primarily involving the formation of iron hydroxide complexes and the dissolution of ions from the material's surface, causing some cavity. According to Guo et al. (2019) and Akinribide et al. (2022), alkaline corrosion can lead to the degradation of ductile iron components, albeit at a slower rate compared to acidic or chloride-rich environments. Fracture surfaces of ductile iron exposed to alkaline NaOH solutions display signs of uniform corrosion, characterized by river makings, smooth etching and surface erosion, as displayed in Fig. 9b. The absence of localized pitting and the presence of oxide/hydroxide films on the fracture surface indicates the gradual dissolution of material due to alkaline attack (Ascencio et al., 2014). Moreover, alkaline environments can also induce some oxide films in ductile iron, particularly under NaOH environmental conditions. Hydrogen atoms generated during the corrosion process can react with the atmosphere causing oxide films deposition on the material's structure, promoting pitting form of corrosion on the surface of the sample (Lynch, 2007; Rajnovic et al., 2008). Fracture surfaces of ductile iron affected by pitting corrosion in alkaline NaOH solutions may exhibit features such as reduced ductility, intergranular cracking, and brittle fracture regions.

In near-neutral environment, as seen in Fig. 9c, the fracture morphology of DI reflects a combination of factors, including corrosion, mechanical loading, and environmental conditions. Fracture surfaces in near-neutral environments may display a mixture of characteristics observed in both acidic and alkaline environments, depending on the specific chemical composition and pH level of the solution (Fierro et al., 2000). Fracture surfaces of ductile iron exposed to near-neutral environments with chloride contamination may exhibit pitting, crevice corrosion, cleavage face, cavity, river markings, and crack initiation sites, as seen in Fig. 9c. All these are indicative of chloride-induced corrosion mechanisms. Overall, fracture morphology analysis of ductile iron immersed in sodium chloride, alkaline NaOH, and near-neutral environments provides valuable insights into the material's response to different chemical conditions.

3.4. Rates of deterioration by weight reduction

At 180 days, three ductile samples were taken out of the environments, and the corrosion rate for these specimens was recorded. After 180 days, it was discovered that the average corrosion rate of the specimens was 0.1 mm/year. From the results, it can be seen that the corrosion rate increased quickly for 180 days, indicating the failure of the materials due to the rates of corrosion increased to 0.1 mm/yr, which is in line with the findings of Song et al. (2017). DI, known for its strength, durability, and versatility, undergoes a fascinating transformation when subjected to weight reduction according to Polishetty (2012). The rates of deterioration experienced in ductile iron was due to weight reduction which are influenced by various factors, including material composition, environmental conditions, and applied stress. One primary mechanism driving deterioration is the reduction in cross-sectional area resulting from weight reduction (Du et al., 2005). As weight is reduced, the thickness of the material decreases, leading to a higher susceptibility to cracking and fracture under mechanical loading (Gouveia et al., 2017). This phenomenon is particularly pronounced in ductile iron structures subjected to cyclic loading or dynamic stresses, such as bridges, pipelines, and automotive components. The passive film may have broken due to chloride ions from the pH solution of all the environment used. For determining the corrosion and its associated impact on the ductile iron samples, a thorough and in-depth technique was used. Adopted for this study. According to the findings of Sherif (2014), weight reduction can accelerate corrosion processes, especially in environments with high moisture and corrosive agents. Thinning of the material exacerbates corrosion, compromising the structural integrity of the iron and hastening its degradation over time. Furthermore, changes in microstructure and grain morphology occur as weight is reduced, affecting the mechanical properties of the material (Jafarian et al., 2021). These alterations can manifest as decreased ductility, increased brittleness, and diminished fatigue resistance, further contributing to the rates of deterioration. Understanding the intricate interplay between weight reduction and deterioration in ductile iron is paramount for designing and maintaining robust infrastructure and industrial components. By employing advanced materials engineering techniques and incorporating mitigation strategies, such as protective coatings and corrosion-resistant alloys, engineers can mitigate the detrimental effects of weight reduction, ensuring the longevity and reliability of ductile iron structures in diverse applications. (Song et al., 2017; Davis, 2000).

According to the findings in Table 1, corrosion produced the change in the ductile iron's composition, which led to the reduction of iron (Fe) and diffusion of corrosive elements. Ferrous metals have also been observed to experience similar compositional changes brought on by corrosive soils in comparable acidic corrosive media (Wasim et al., 2019a, 2019b, 2020c, 2020d). Other ferrous metals showed a decrease in the phases, specifically the ferrite and pearlite phases of the specimens, which ultimately led to a decrease in the bulk mechanical parameters including ultimate tensile (Wasim et al., 2019b, 2020d), and fatigue strength (Wasim et al., 2020c; Wang et al., 2018). In contrast to flaky graphite-shaped cast iron, which is fragile, ductile iron is a type of cast iron where the graphite is shaped like nodules, making it harder. Recently, the bulk mechanical characteristics of pipes composed of flaky graphite have been reported to degrade in an environment with acidic soil (Wang et al., 2019; Anadebe et al., 2022). Similarly, corrosion can affect the mechanical characteristics of ductile iron in its bulk. However, a notable drop in the mechanical characteristics of the ductile iron grains was set in, indicating that corrosion clearly affects mechanical characteristics. The outcomes are consistent with the most recent research on the corrosive soil-induced degradation of the granular nanomechanical characteristics of cast iron (Wasim et al., 2021). Ductile iron samples were employed in the current study to see the shift in microstructural characteristics brought on by the corrosive environment.

Table 4
Statistical properties of the input and output variables.

	Input			Output	
	Exposure time (days)	Weight (g)	Environment	Corrosion rate	hardness
Maximum	180.00	20.80	+	0.02400	1341.00
Minimum	1.00	20.42	+	0.00033	21.00
Mean	90.14	20.62	+	0.01210	681.00
St.D	64.57	0.15	+	0.00930	426.94

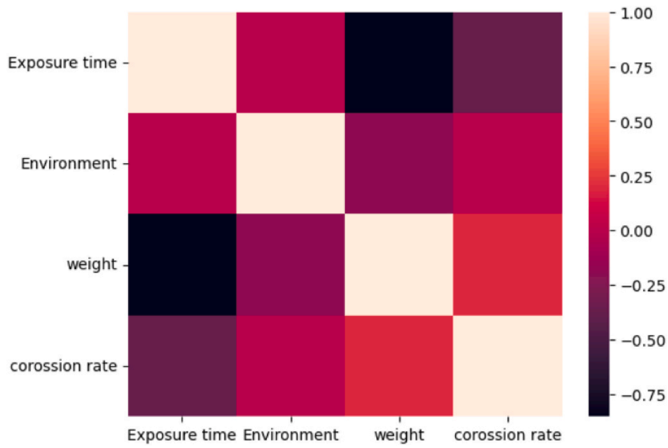

Fig. 10. Correlation heat map of the input variables with the corrosion rates.

3.5. Performance outcome of the ANFIS-PSO model

The data used for developing the hybrid model were extracted from the experimental proceedings. Table 4 represents the statistical summary of the data. The heat map in Fig. 10 represents the correlation between the variables.

The computational advantage and flexibility of the neuro-fuzzy model which allows variation of its hyper-parameters to achieve optimality in the model has been explored in the present study (Adegoke et al., 2022; Kilani et al., 2022; Anadebe et al., 2020). Further to this, the significant effect of the parameter tuning of the neuro-fuzzy models using evolutionary algorithms such as the PSO for optimal performance of ANFIS was established in this study. The comparative analysis of the predictive capacity of the different clustering techniques of the hybrid ANFIS-PSO involving fuzzy c-means (FCM), grid partitioning (GP) and subtractive clustering (SC) were carried out.

Several trials of training were carried out until an optimal hybrid ANFIS-PSO models that give the minimum error and highest accuracy were obtained. It was ensured that over fitting and under fitting are avoided to ascertain that the optimal models learn the data rather than memorizing and fail during the model testing phase. The optimal model architectures were tested with both the training and testing data. Presented in Table 5 are the statistical metrics result of the optimal ANFIS-PSO model based on different clustering techniques at the testing and training phase for corrosion rate of ductile iron. Based on all metrics used for assessing the models' performance, a better prediction was observed in the ANFIS-PSO result based on FCM clustering than the other clustering as it gave the least prediction error and highest accuracy. The ANFIS-PSO result is 93.7% and 87.6% accurate at the training and testing phase respectively based on MAPE-values ($MAPE_{training} = 6.386, MAPE_{testing} = 12.456$) compared to the ANFIS standalone model which is 92.9% and 87.1% accurate at the training and testing phase ($MAPE_{training} = 7.124, MAPE_{testing} = 12.975$). A significant variation was noted in the RMSE values of the ANFIS-PSO using different clustering approaches. Both at the testing and training phase, a lower RMSE was recorded for the ANFIS-PSO depicting a more reliable and accurate model. The RMSE and MAD values of ANFIS-PSO are 0.0786 and 0.3245, thus revealing the eligibility and capability of the model. A strong agreement between the experimental and predicted values of corrosion rates was demonstrated in the R^2-values of all models, while the highest value of ANFIS-PSO-FCM was validates its better performance than others.

Shown in Table 6 is the statistical metrics result of the ANFIS-PSO model based FCM, GP and SC clustering techniques for hardness of the ductile iron based on weight loss method. A lower variability was also noted in the values of the experimental and predicted values of the hardness as lower prediction errors and higher accuracies were recorded for all models at the testing and training phase. Based on the RMSE, MAD and MAPE values, ANFIS-PSO model using FCM technique had the best performance in predicting the hardness of the ductile iron. The RMSE ($RMSE_{training} = 0.1248, RMSE_{testing} = 0.1887$) and MAD values of the model ($MAD_{training} = 0.2456, MAD_{testing} = 0.5385$) revealed its reliability and eligibility in outcome prediction. The R^2-values at the testing phase showed a stronger agreement between the experimental and predicted values of hardness of the ductile iron.

The prediction outcome of the ANFIS-PSO model based on all the clustering techniques for the tensile strength is reasonable as the models predicted with lesser errors based on RMSE and MAD-values and higher accuracies based on MAPE, and R^2-values as shown in Table 7. The MAD-value ($MAD_{ANFIS-PSO-FCM} = 0.4627$) at the testing phased demonstrated a lower variability in the predicted outcomes and lower positive distance between the predicted outcomes and the mean values of tensile strength. The eligibility and reliability of the developed ANFIS-PSO-FCM models in predicting the tensile strength were demonstrated by their RMSE-values ($RMSE_{ANFIS-PSO-FCM} = 0.4627$) at the testing phase. The RMSE-values further depicted a good spread of the prediction outcomes around the residuals, and thus giving an acceptable fit between the models and predicted outcomes of tensile strength. The training of the ANFIS-PSO-FCM is 93.3% accurate ($MAPE_{ANFIS-PSO-FCM} = 0.4627$), while at the testing phase, the models is 88.7% accurate ($MAPE_{ANFIS-PSO-FCM} = 11.321$).

Tables 5–7 respectively present the predicted values of the corrosion rate, harness and tensile strength of the ductile iron based on the exposure time, environment and weight loss using the FCM-clustered ANFIS standalone and FCM-clustered PSO-ANFIS model. Laudable outcomes were recorded for both models as closer range values were observed in the experimental and predicted values of corrosion rate. Both models recorded with a minimal prediction error, however a lower prediction error was observed for the ANFIS-PSO-FCM than the standalone model. The percentage error of the ANFIS-PSO-FCM predictions is significantly lower than the ANFIS-standalone prediction. This shows that the ANFIS-PSO-FCM performed better than the ANFIS standalone models for predicting all the outcomes.

Tables 8–10 respectively display the comparison between experimental values and predicted values for corrosion rates with some discrepancies due to factors such as surface imperfections, localized corrosion effects, or variations in environmental conditions. Additionally, the predictive model's accuracy may be limited by the complexity of corrosion processes and the difficulty in capturing all influencing

Table 5
Statistical metrics result of ANFIS-PSO for corrosion rate.

Model	Clustering		Performance metrics			
			RMSE	MAD	MAPE	R^2
ANFIS-PSO	FCM	Training	0.0521	0.1532	7.124	0.9675
		Testing	0.0806	0.4532	12.975	0.9402
	SC	Training	0.0634	0.2352	8.051	0.9235
		Testing	0.0842	0.5106	11.246	0.9134
	GP	Training	0.6973	0.2557	9.526	0.9134
		Testing	0.0885	0.4262	13.612	0.9426

Table 6
Statistical metrics result of ANFIS-PSO for hardness.

Model	Clustering		Performance metrics			
			RMSE	MAD	MAPE	R^2
ANFIS-PSO	FCM	Training	0.1248	0.2456	8.2374	0.9847
		Testing	0.1887	0.5385	15.4683	0.9532
	SC	Training	0.1346	0.7433	9.1054	0.9653
		Testing	0.1863	0.5576	17.733	0.9445
	GP	Training	0.1402	0.5214	9.056	0.9235
		Testing	0.1892	0.5731	16.879	0.9135

Table 7
Statistical metrics result of ANFIS-PSO for tensile strength.

Model	Clustering		Performance metrics			
			RMSE	MAD	MAPE	R^2
ANFIS-PSO	FCM	Training	0.0773	0.1751	6.745	0.9725
		Testing	0.0953	0.4627	11.321	0.9467
	SC	Training	0.0756	0.2453	8.334	0.9503
		Testing	0.0967	0.8545	13.043	0.9356
	GP	Training	0.0823	0.2432	7.894	0.9542
		Testing	0.0984	0.8781	12.042	0.9214

factors. Further refinement of predictive models for ductile iron corrosion rates may involve incorporating additional parameters, refining experimental techniques, or considering the synergistic effects of multiple variables. Validation of the model against a broader range of experimental data is also crucial for enhancing its accuracy and reliability.

The experimental and predicted microhardness values show some little different behaviour which is attributable to differences in sample preparation, measurement techniques, or the influence of microstructural features on hardness. Calibration of the predictive model using a broader range of experimental data and finer resolution in input parameters may improve its predictive capability while the experimental and predicted tensile behavior display inconsistencies due to factors such as strain rate effects, temperature variations, or material anisotropy. The predictive model's accuracy may be limited by the complexity of material deformation mechanisms and the difficulty in accurately capturing all influencing factors.

The comparison plot of experimental and predicted values of corrosion rates, hardness and tensile strength respectively using the 30% hold out test sample data are represented in Fig. 11 below. The figures depict a strong agreement between the experimental data and the predicted values with a marginal variations and less misprediction. A similar trend exists between the predicted data and experimental data for both optimal ANFIS and ANFIS-PSO which gave the best prediction outcomes. The few under-predictions and over-predictions could be

Table 8
Experimental and predicted outcome of the corrosion rate of ductile iron.

Exposure time	Environment	Weight loss	Corrosion rate				
			Experimental	ANFIS-FCM		ANFIS-PSO-FCM	
				Predicted	Error (%)	Predicted	Error (%)
30	1	20.65	0.02429	0.02655	8.49	0.02546	0.67
30	2	20.59	0.00480	0.00487	1.36	0.00465	1.04
30	3	20.63	0.00039	0.00035	3.34	0.00042	4.81
60	1	20.61	0.00033	0.00036	9.73	0.00032	2.73
60	2	20.59	0.02429	0.02564	5.24	0.02479	1.98
60	3	20.57	0.00400	0.00416	3.67	0.00412	0.49
90	1	20.56	0.00047	0.00049	4.65	0.00055	2.27
90	2	20.57	0.01203	0.01244	3.32	0.01366	1.09
90	3	20.50	0.00028	0.00031	6.75	0.00280	3.14
120	1	20.51	0.00099	0.00098	0.23	0.00099	0.35
120	2	20.56	0.00035	0.00034	1.63	0.00036	0.99
120	3	20.44	0.00601	0.00608	1.15	0.00612	0.09
150	1	20.47	0.02429	0.02475	1.81	0.02543	1.00
150	2	20.56	0.00069	0.00068	3.03	0.00075	3.48
150	3	20.37	0.00023	0.00023	0.04	0.00025	5.26
180	1	20.42	0.00066	0.00069	5.57	0.00065	0.91
180	2	20.55	0.00049	0.00047	6.34	0.00051	9.67
180	3	20.31	0.00802	0.00818	1.98	0.00800	0.67

Environments (1- Near neutral Environment, 2 – Alkaline NaOH, 3- NaCl)

Table 9
Experimental and Predicted outcome of the hardness of ductile iron.

Exposure time	Environment	Weight loss	Hardness				
			Experimental	ANFIS-FCM		ANFIS-PSO-FCM	
				Predicted	Error (%)	Predicted	Error (%)
30	1	20.65	1341.72	1372.343	2.23	1343.634	0.14
30	2	20.59	188.74	200.964	6.08	190.754	1.05
30	3	20.63	272.53	291.975	6.66	294.753	7.54
60	1	20.61	544.57	580.643	6.21	576.754	5.58
60	2	20.58	345.29	370.754	6.89	366.975	5.91
60	3	20.57	943.15	1000.643	5.74	985.755	4.32
90	1	20.56	363.59	397.966	8.63	376.423	3.41
90	2	20.57	356.31	390.544	8.76	384.633	7.36
90	3	20.50	1142.44	1152.555	0.88	1146.233	0.33
120	1	20.51	21.17	23.235	8.91	22.545	6.12
120	2	20.56	403.45	447.343	9.80	407.435	0.98
120	3	20.44	343.66	349.743	1.74	345.865	0.64
150	1	20.47	423.37	463.543	8.66	452.555	6.44
150	2	20.56	383.52	410.544	6.58	406.343	5.62
150	3	20.37	20.62	22.534	8.49	21.544	4.28
180	1	20.42	323.73	357.977	9.57	344.754	6.09
180	2	20.55	104.95	115.635	9.24	113.535	7.56
180	3	20.31	743.86	790.864	5.94	778.976	4.51

Environments (1- Near neutral Environment, 2 – Alkaline NaOH, 3- NaCl)

Table 10
Experimental and predicted outcome of the tensile strength.

Exposure time	Environment	Weight loss	Tensile Strength				
			Experimental	ANFIS-FCM		ANFIS-PSO-FCM	
				Predicted	Error (%)	Predicted	Error (%)
30	1	20.65	488.45	2849.75	1.01	2809.75	1.02
30	2	20.59	605.00	845.45	0.83	805.45	0.87
30	3	20.63	617.99	589.64	1.64	627.643	1.54
60	1	20.61	643.44	2012.57	0.47	2009.57	0.47
60	2	20.58	990.89	1129.57	0.37	1112.57	0.37
60	3	20.57	1158.75	2587.57	2.76	2571.567	2.78
90	1	20.56	798.42	1198.65	0.15	1160.65	0.16
90	2	20.57	1200.00	616.48	1.38	596.48	1.42
90	3	20.50	1699.50	3352.16	0.58	3341.16	0.58
120	1	20.51	953.41	1281.76	0.96	1275.76	0.97
120	2	20.56	2000.02	3028.68	0.38	3011.67	0.39
120	3	20.44	2240.25	506.47	0.79	492.47	0.82
150	1	20.47	1108.39	663.54	1.07	650.54	1.09
150	2	20.56	2500.05	2287.33	0.75	2257.33	0.75
150	3	20.37	2781.00	1711.76	0.24	1703.76	0.25
180	1	20.42	1263.38	1219.46	0.94	1211.45	0.94
180	2	20.55	3000.05	980.53	2.05	973.53	2.07
180	3	20.31	3321.75	1010.57	1.06	1001.57	1.07

Environments (1- Near neutral Environment, 2 – Alkaline NaOH, 3- NaCl).

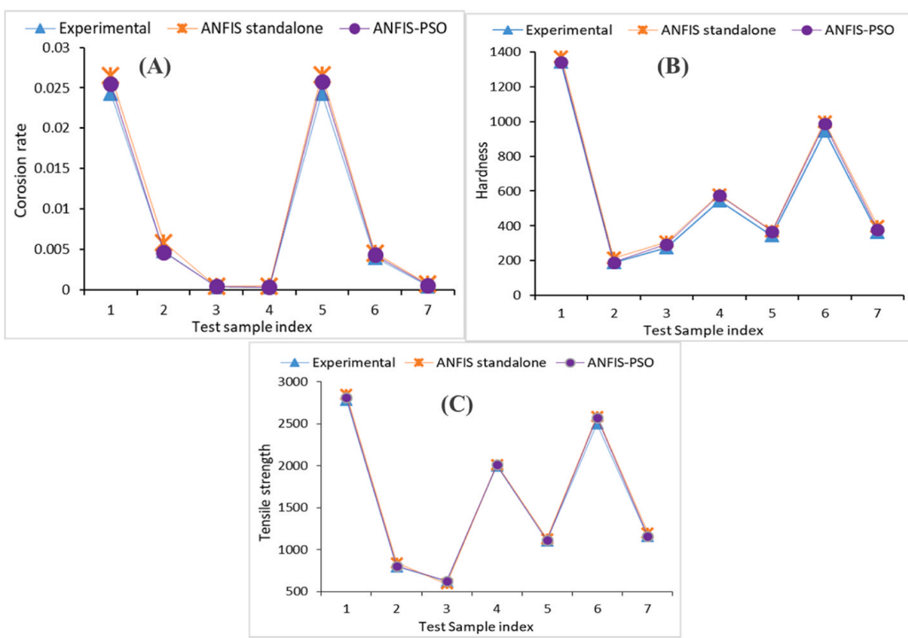

Fig. 11. Comparison test plot of the experimental and (A) predicted corrosion rates, (B) predicted hardness and, (C) predicted tensile strength.

attributed to the under-estimations and over-estimations of some of the parameters of the algorithms (Adeleke et al., 2022b; Taofeeq et al., 2020; Anadebe et al., 2022)

From the experimental study, we subject DI samples to corrosion tests, hardness measurements, and tensile strength tests. The corrosion tests were conducted in a controlled environment simulating real-world conditions, such as near-neutral, alkaline sodium hydroxide (NaOH), and sodium chloride (NaCl) environments for 180 days. Hardness measurements were performed using standard techniques like Vickers hardness tests. Tensile strength tests involved applying tensile loads to the ductile iron until failure, following ASTM E8 standards according to Baboian et al. (Baboian, 2005).

Predictive models for corrosion rates, hardness, and tensile strength were developed based on theoretical frameworks and empirical data as seen in Fig. 11(a–c). These models incorporate factors such as material composition, environmental conditions, and processing methods. The experimental results from this study were used to validate a model generated using hybrid adaptive neuro-fuzzy inferences system-particle swarm optimization (ANFIS-PSO) algorithms. The hybrid ANFIS-PSO modelling technique was improved for a detailed evaluation of corrosion rate of ductile cast iron materials in different environments. The integrated hybrid ANFIS-PSO model revealed a sharp rise in localized corrosion caused by chloride-induced structural deterioration at the nanoscale for some of the grains may have been employed to establish correlations between input parameters and material properties (Mosavi et al., 2019).

The comparison between experimental and predicted corrosion rates in Fig. 11a revealed a close agreement in some cases but discrepancies in others. Factors such as the presence of surface imperfections, localized corrosion effects, or unforeseen environmental variables could contribute to these disparities (Callister et al., 2007). Further refinement of the predictive model may be necessary to enhance its accuracy, potentially by incorporating additional parameters or refining the experimental setup. The comparison of experimental and predicted hardness values in Fig. 11b exhibited varying degrees of agreement. Deviations arise due to differences in sample preparation, measurement techniques, or the influence of microstructural features on hardness. Calibration of the predictive model using a broader range of experimental data and finer resolution in input parameters may improve its predictive capability. Comparing experimental tensile strength with predicted values in Fig. 11c revealed trends similar to those observed for corrosion rates and hardness.

While the predictive model, according to Mosavi et al. (2019), might capture the general behavior of the material, discrepancies between predicted and experimental values highlight the need for further validation and refinement. Factors such as strain rate effects, temperature variations, and material anisotropy could influence tensile strength predictions and require consideration in the model. The comparison of experimental and predicted material properties provides valuable insights into the accuracy and reliability of predictive models. Discrepancies between experimental and predicted values highlight the limitations of current models and the complexities involved in accurately forecasting material behavior (Callister et al., 2007). Future research efforts should focus on refining predictive models through iterative experimentation, incorporating additional influencing factors, and enhancing model strength.

4. Conclusion

The structural integrity of DI components is crucial for the safety, reliability, and longevity of engineering systems, and understanding their corrosion behavior in different environments is essential for mitigating corrosion-related risks and ensuring optimal performance. This study used aqueous NaOH, NaCl, and near neutral solution electrolytes to evaluate three selected DI specimens. The experimental results were analyzed using the ANFIS-PSO model, which predicted the corrosion rate and mechanical properties of the DI specimens in the different test environments. Due to the nodular graphite ferritic microstructure and high silicon concentration, the DI specimen subjected to NaOH and near neutral environment exhibited the least corrosion rate at 0.0019 and 0.0021 mmy^{-1} respectively compared to 0.0022 mmy^{-1} for DI sample in NaCl environment. The results obtained for experimental, ANFIS standalone and ANFIS-PSO were all similar in trends. Moreover, the enhanced resistance to corrosion exhibited by the DI specimens in these environments was also ascribed to the formation of pseudo-passive layers on their surfaces, reducing the attack of the aggressive ions in the electrolyte. A hybrid ANFIS-PSO modeling was performed by using exposure time, environment, and weight loss as the input parameters to predict the corrosion rate, tensile strength, and hardness. The percentage error recorded in the ANFIS-PSO predictions was significantly lower than the ANFIS-standalone prediction, which confirmed that the ANFIS-PSO had a better performance than the ANFIS standalone models. This finding is especially crucial for corrosion monitoring technology's long-term survival and financial stability. However, there is still a need for thorough corrosion assessment methodologies and further investigations, such as electrochemical impedance spectroscopy (EIS), may enhance comprehension of the process by furnishing additional data for modeling.

Declaration of competing interest

The authors declare that they have no known competing financial interests or personal relationships that could have appeared to influence the work reported in this paper.

Acknowledgements

The authors would like to express their gratitude to the University Study Committee (URC) funding and the Centre for Nanoengineering and Advanced Materials at the University of Johannesburg aid in creating a suitable study environment were also acknowledged by the authors. The Engineering Materials Development Institute (EMDI), Akure employees and our research lab coworkers were really helpful.

References

Adegoke, K.A., Maxakato, N.W., 2022. Porous metal oxide electrocatalytic nanomaterials for energy conversion: oxygen defects and selection techniques. Coord. Chem. Rev. 457, 214389.
Adeleke, O., et al., 2022a. Prediction of the heating value of municipal solid waste: a case study of the city of Johannesburg. Int. J. Ambient Energy 43 (1), 3845–3856.
Adeleke, O., et al., 2022b. Prediction of municipal solid waste generation: an investigation of the effect of clustering techniques and parameters on ANFIS model performance. Environ. Technol. 43 (11), 1634–1647.
Akinribide, O.J., et al., 2022. A review on heat treatment of cast iron: phase evolution and mechanical characterization. Materials 15 (20), 7109.
Anadebe, V.C., et al., 2020. Electrochemical-kinetics, MD-simulation and multi-input single-output (MISO) modeling using adaptive neuro-fuzzy inference system (ANFIS) prediction for dexamethasone drug as eco-friendly corrosion inhibitor for mild steel in 2 M HCl electrolyte. J. Taiwan Inst. Chem. Eng. 115, 251–265.
Anadebe, V.C., et al., 2022. Sulfur-doped graphitic carbon nitride (Sg-C3N4) as an efficient corrosion inhibitor for X65 pipeline steel in CO2-saturated 3.5% NaCl solution: electrochemical, XPS and Nanoindentation Studies. Process Saf. Environ. Protect. 164, 715–728.
Ascencio, M., Pekguleryuz, M., Omanovic, S., 2014. An investigation of the corrosion mechanisms of WE43 Mg alloy in a modified simulated body fluid solution: the influence of immersion time. Corrosion Sci. 87, 489–503.
Astm, G., Practice for Preparing. Cleaning and Evaluating Corrosion Test Specimens..
Baboian, R., 2005. Corrosion Tests and Standards: Application and Interpretation, vol. 20. ASTM international.
Bamgbade, J., et al., 2022. Building sustainability in the construction industry through firm capabilities, technology and business innovativeness: empirical evidence from Malaysia. International journal of construction management 22 (3), 473–488.
Callister, W.D., et al., 2007. Materials Science and Engineering: an Introduction, vol. 7. John wiley & sons, New York.
Davis, J.R., 2000. Corrosion: Understanding the Basics. Asm International.
Du, Y., Clark, L., Chan, A., 2005. Residual capacity of corroded reinforcing bars. Mag. Concr. Res. 57 (3), 135–147.
Eberhart, R., Kennedy, J., 1995. A new optimizer using particle swarm theory. In: MHS'95. Proceedings of the Sixth International Symposium on Micro Machine and Human Science. Ieee.
Fierro, V., et al., 2000. *Comportamiento mecánico de fundiciones esferoidales entre À100 C y 200 C*. in *Congreso binacional de metalurgia y materiales SAM/CONAMET—IV Coloquio Latinoamericano de Fractura y Fatiga*. Neuquén Argentina.
Gouveia, R.M., et al., 2017. Study of the heat-treatments effect on high strength ductile cast iron welded joints. Metals 7 (9), 382.
Guo, S., et al., 2019. A critical review of corrosion development and rust removal techniques on the structural/environmental performance of corroded steel bridges. J. Clean. Prod. 233, 126–146.
Jafarian, H., et al., 2021. The influence of austenitization temperature on microstructural developments, mechanical properties, fracture mode and wear mechanism of Hadfield high manganese steel. J. Mater. Res. Technol. 10, 819–831.
Jang, J.-S.R., 1993a. Department of electrical engineering and computer science university of California, berkeley, CA 94720. In: IEEE Trans. On Systems, Man and Cybernetics, vol. 23, pp. 665–685.
Jang, R., 1993b. 'ANFIS: adaptive neuro fuzzy inference system'. IEEE Transactions on System, Man, and Cybernetics 23 (3).
Joseph, O.O., et al., 2021. Corrosion resistance of galvanized roofing sheets in acidic and rainwater environments. Heliyon 7 (12).
Kilani, M., Diop, N., De Wolf, D., 2022. A multimodal transport model to evaluate transport policies in the North of France. Sustainability 14 (3), 1535.
Kleiner, Y., Rajani, B., Krys, D., 2012. Performance of ductile iron pipes. I: characterization of external corrosion patterns. J. Infrastruct. Syst. 61.
Koch, G.H., et al., 2005. Cost of corrosion in the United States. In: Handbook of Environmental Degradation of Materials. Elsevier, pp. 3–24.
Koneshan, S., Rasaiah, J.C., 2000. Computer simulation studies of aqueous sodium chloride solutions at 298 K and 683 K. J. Chem. Phys. 113 (18), 8125–8137.
Krawiec, H., et al., 2021. In-situ monitoring of the corrosion behaviour of austempered ductile iron (ADI) under cyclic salt spray exposure. Corrosion Sci. 185, 109437.
Labrecque, C., Gagne, M., 1998. Ductile iron: Fifty years of continuous development. Can. Metall. Q. 37 (5), 343–378.
Lazreg, M., Benamrane, N., 2022. Hybrid system for optimizing the robot mobile navigation using ANFIS and PSO. Robot. Autonom. Syst. 153, 104114.
Li, B., et al., 2022. Viral infection and transmission in a large, well-traced outbreak caused by the SARS-CoV-2 Delta variant. Nat. Commun. 13 (1), 1–9.
Lynch, S., 2007. Progress towards Understanding Mechanisms of Hydrogen Embrittlement and Stress Corrosion Cracking. NACE CORROSION. NACE-07493.
Mosavi, A., Bahmani, A., 2019. Energy consumption prediction using machine learning; a review.
Ochoa, N., et al., 2022. Pseudo-passive films on cast irons: a strategy to mitigate corrosion by acting directly on microstructure. Corrosion Sci. 206, 110480.

Polishetty, A., 2012. Machinability and Microstructural Studies on Phase Transformations in Austempered Ductile Iron. Auckland University of Technology.
Qin, M., et al., 2018. Corrosion behavior of 9% Ni steel for LNG storage tanks in 3.5 wt.% NaCl solution. Int. J. Electrochem. Sci. 13, 6537–6549.
Rajaobelina, L., et al., 2022. Examining emotions linked to live chat services: the role of e-service quality and impact on word of mouth. J. Financ. Serv. Market. 27 (3), 232–249.
Rajnovic, D., Eric, O., Sidjanin, L., 2008. Transition temperature and fracture mode of as-castand austempered ductile iron. Journal of microscopy 232 (3), 605–610.
Romanoff, M., 1957. Underground Corrosion, vol. 579. US Government Printing Office.
Seifi, A., et al., 2022. Multi-model ensemble prediction of pan evaporation based on the Copula Bayesian Model Averaging approach. Eng. Appl. Artif. Intell. 114, 105124.
Sherif, E.-S.M., 2014. The role of corrosion inhibitors in protecting metallic structures against corrosion in harsh environments. The role of colloidal systems in environmental protection 509–526.
Song, Y., et al., 2017. Raman-Deuterium Isotope Probing for in-situ identification of antimicrobial resistant bacteria in Thames River. Sci. Rep. 7 (1), 1–10.
Szeliga, M.J., Simpson, D.M., 2003. Evaluating ductile iron pipe corrosion. In: New Pipeline Technologies, Security, and Safety, pp. 115–129.
Taofeeq, D., Adeleke, A.Q., Lee, C.-K., 2020. The synergy between human factors and risk attitudes of Malaysian contractors': moderating effect of government policy. Saf. Sci. 121, 331–347.
Wang, W., et al., 2018. Experimental investigation on corrosion effect on mechanical properties of buried cast iron pipes. J. Mater. Civ. Eng. 30 (8), 04018197.
Wang, W., Li, C.-Q., Shi, W., 2019. Degradation of mechanical property of corroded water pipes after long service. Urban Water J. 16 (7), 494–504.
Wasim, M., et al., 2017. Corrosion behaviour of pipes in soil and in simulated soil solution. Corrosion and prevention 1–12.
Wasim, M., et al., 2018. Factors influencing corrosion of metal pipes in soils. Environ. Chem. Lett. 16 (3), 861–879.
Wasim, M., et al., 2019a. Quantitative study of coupled effect of soil acidity and saturation on corrosion and microstructure of buried cast iron. J. Mater. Civ. Eng. 31 (9), 04019206.
Wasim, M., et al., 2019b. Mechanical and microstructural evaluation of corrosion and hydrogen-induced degradation of steel. J. Mater. Civ. Eng. 31 (1), 04018349.
Wasim, M., et al., 2020a. Effect of soil's acidity and saturation on degradation of fracture toughness of buried cast iron. J. Mater. Civ. Eng. 32 (7), 04020180.
Wasim, M., et al., 2020b. Correlation model for the corrosion rates of buried cast iron pipes. J. Mater. Civ. Eng. 32 (12), 04020353.
Wasim, M., et al., 2020c. Fracture toughness degradation of cast iron due to corrosive mediums. Int. J. Pres. Ves. Pip. 186, 104151.
Wasim, M., Ngo, T.D., 2020d. Failure analysis of structural steel subjected to long term exposure of hydrogen. Eng. Fail. Anal. 114, 104606.
Wasim, M., Robert, D., Li, C.-Q., 2021. Corrosion effects on the granular nano mechanical properties of buried cast iron. Eng. Fail. Anal. 119, 104970.
You, Z., et al., 2020. Influence of water and sodium chloride content on corrosion behavior of cast iron in silty clay. Construct. Build. Mater. 238, 117762.
Zhang, X., et al., 2011. In situ Raman spectroscopy study of corrosion products on the surface of carbon steel in solution containing Cl− and SO42. Eng. Fail. Anal. 18 (8), 1981–1989.
Zheng, B., et al., 2020. Effect of chromium-induced (Fe, Cr) 3C toughness improvement on the two-body abrasive wear behaviors of white cast iron. Wear 456, 203363.